PHOTONICS Research

Ultracompact silicon on-chip polarization controller

Weike Zhao,[1,†] Yingying Peng,[1,†] Mingyu Zhu,[1] Ruoran Liu,[1] Xiaolong Hu,[2,3] Yaocheng Shi,[1] and Daoxin Dai[1,4,*]

[1]*State Key Laboratory for Modern Optical Instrumentation, Center for Optical & Electromagnetic Research, College of Optical Science and Engineering, International Research Center for Advanced Photonics, Zhejiang University, Zijingang Campus, Hangzhou 310058, China*
[2]*School of Precision Instrument and Optoelectronic Engineering, Tianjin University, Tianjin 300072, China*
[3]*Key Laboratory of Optoelectronic Information Science and Technology, Ministry of Education, Tianjin 300072, China*
[4]*Ningbo Research Institute, Zhejiang University, Ningbo 315100, China*
[†]*These authors contributed equally to this work.*
Corresponding author: dxdai@zju.edu.cn

On-chip polarization controllers are extremely important for various optical systems. In this paper, a compact and robust silicon-based on-chip polarization controller is proposed and demonstrated by integrating a special polarization converter and phase shifters. The special polarization converter consists of a 1×1 Mach–Zehnder interferometer with two polarization-dependent mode converters at the input/output ends. When light with an arbitrary state of polarization (SOP) is launched into the chip, the TE_0 and TM_0 modes are simultaneously excited. The polarization extinction ratio (PER) and the phase difference for the TE_0/TM_0 modes are tuned by controlling the first phase shifter, the polarization converter, and the second phase shifter. As a result, one can reconstruct the light SOP at the output port. The fabricated polarization controller, as compact as $\sim 150~\mu m \times 700~\mu m$, exhibits an excess loss of less than 1 dB and a record PER range of >54 dB for arbitrary input light beams in the wavelength range of 1530–1620 nm. © 2024 Chinese Laser Press

1. INTRODUCTION

State of polarization (SOP), as the fundamental property of light, has been extensively studied and utilized for various applications, such as telecommunications [1,2], optical coherence tomography [3], medical diagnosis [4], light remote detection and ranging (lidar) [5,6], and material analysis [7]. The polarization-controlling devices have been heavily investigated as the crucial role in polarization management. Traditionally, polarization management is often achieved by mechanically rotating the wave plates or utilizing the fiber-squeezing birefringence effect [8,9]. Unfortunately, they are bulky, low-speed, and poorly programmable/reconfigurable.

As an alternative, on-chip polarization controllers (PCs) are becoming more and more attractive and feasible because integrated photonics has been developed very successfully with various materials platforms in the past decades [10,11]. In particular, silicon, InP, SiN, and thin-film lithium niobate photonic waveguides with ultrahigh index contrasts usually offer high birefringence and thus provide extremely powerful options for realizing on-chip polarization-handling devices [12–14]. Currently, various high-performance on-chip polarization-handling devices have been realized successfully, including

polarization rotators [15–17], polarization beam splitters [18–20], and polarization splitting rotators (PSRs) [21–24]. Moreover, on-chip PCs have also been developed by utilizing the thermo-optic effect [25], the carrier dispersion effect [26], and the electro-optic effect [27], featuring the excellence of reconfigurability, high-speed operation, and low-power dissipation. With high-performance PCs, one can realize the generation/conversion of SOP [25,27–31], automatic polarization calibration [32,33], polarization scrambling [27], and polarization measurement [26,27,34], which have been playing a vital role in many scenarios such as optical communication [35], optical sensing [36,37], and quantum technology [29,38,39].

Generally speaking, there are mainly two schemes to achieve on-chip polarization controlling. One is using the combination of PSRs and 2×2 Mach–Zehnder interferometers (MZIs) [31–33,40]. In these designs, the PSRs separate/combine the TE_0 and TM_0 modes, while the MZIs tune the polarization extinction ratio (PER) or the phase difference for the TE_0 and TM_0 modes. In Ref. [25], a silicon PC was proposed to achieve the conversion of two arbitrary SOPs. In order to eliminate the negative influence from the non-ideality of the PSRs and the 2×2 multimode interferometers (MMIs) used for the

MZIs, five heaters were introduced for thermal-tuning. As a result, the total length is longer than ∼2500 μm and the excess loss (EL) is higher than ∼4.5 dB. Similarly, a PC based on thin-film lithium niobate photonic waveguides was also demonstrated with a PER range of 41.9 dB and an EL of ∼0.92 dB [27]. This design still includes multistage MZIs, and thus the total length is as long as 4.5 cm. As an alternative, the combination of polarization rotators (PRs) and phase shifters (PSs) [28,30] provides another option for achieving on-chip polarization controlling. The PRs provide the ability to modify the PER, while the PS enables the controlling of the phase difference. In this way, the demonstrated PC exhibits a PER range of about 40 dB and a total length of >3000 μm. Therefore, the realization of compact PCs with high performance is still challenging.

In this paper, we propose and demonstrate a compact and robust silicon-based on-chip PC that consists of a special polarization converter and two phase shifters (PSs). These two PSs are connected with the input and output ports of the polarization converter, respectively, to adjust the phase difference between the two orthogonal polarization modes (i.e., TE_0 and TM_0 modes). The special polarization converter is designed with a structure similar to our previous polarization switch used for switching the TE_0 and TM_0 modes [41], and it consists of a 1×1 MZI integrated with two polarization-dependent mode converters (PDMCs) at the input/output ends. In particular, the 1×1 MZI is configured with two thermally tunable PSs embedded in its arms and two 1×2 dual-mode 3-dB power splitters (DMPSs) based on a triple-core adiabatic taper [41]. When light with an arbitrary SOP is launched into the chip, the TE_0 and TM_0 modes are simultaneously excited with the corresponding PER and phase difference (depending on the initial SOP of light). The PER and the phase difference of the TE_0/TM_0 modes can be adjusted freely by tuning the three PSs so that the SOP of light emitted from the chip can be

controlled flexibly. The fabricated PC has a footprint of ∼150 μm × 700 μm, an on-chip EL of ∼1 dB, and a record PER range of >54 dB in the wavelength range of 1530–1620 nm. The present on-chip controller shows high performance regarding configuration compactness and controlling simplicity, which is very attractive and useful for further monolithic photonic integration in the future.

2. PRINCIPLE AND DESIGN

The electric vector motion trail of a plane light wave is described as the following form:

$$\begin{cases} E_x = a_x e^{-i(\omega t + \delta_x)} \\ E_y = a_y e^{-i(\omega t + \delta_y)} \end{cases}, \tag{1}$$

in which E_x and E_y are the horizontal and vertical electrical components of the plane light wave, $a_{x,y}$ are their corresponding amplitudes, $\delta_{x,y}$ are their initial phases, ω is the angular frequency, and t is time. The light SOP is usually characterized by the PER defined as $10 \log_{10}(a_y^2/a_x^2)$ and the phase difference δ_0 given by $\delta_y - \delta_x$. It can be seen that the light SOP can be controlled freely when tuning the PER and the phase difference δ_0.

Figure 1(a) shows the proposed on-chip PC, which consists of a special polarization converter, two PSs (i.e., PS #1 and PS #3), and two edge couplers. Particularly, the polarization converter consists of an MZI connected with two PDMCs (i.e., PDMC #1 and PDMC #2) at the input/output ends. Here the MZI is constructed with two 1×2 DMPSs (i.e., DMPS #1 and DMPS #2) and two thermally-tunable PSs (i.e., PS #2a and PS #2b) embedded in the MZI arms. With the PDMC based on the polarization-dependent mode hybridity [41,42], the launched TM_0 mode is efficiently converted into the TE_1 modes, while the launched TE_0 mode
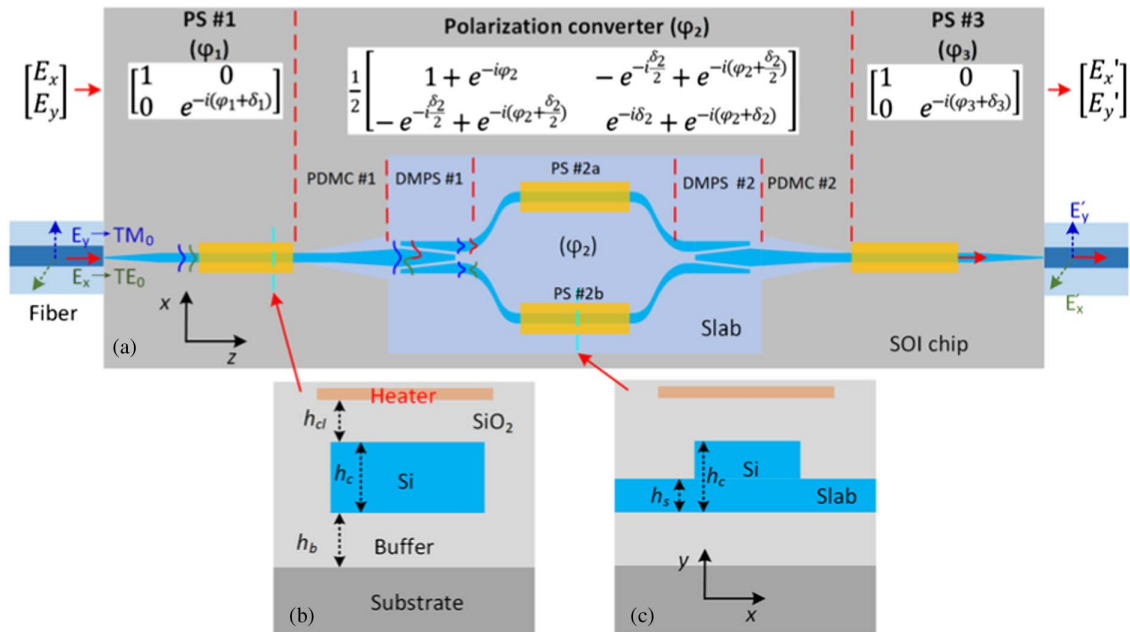
Fig. 1. Schematic configuration of the proposed on-chip PC. (a) Top view; (b) waveguide cross section of PS #1 and PS #3; (c) waveguide cross section of PS #2.

is kept unchanged losslessly in theory. The DMPS is designed with a trident waveguide structure based on the principle of adiabatic mode evolution [41]. Accordingly, the TE_0 mode is uniformly split into two TE_0 modes with identical phases, while the TE_1 mode is uniformly split into two TE_0 modes with a phase difference of π. PS #2a and PS #2b are used to achieve the desired phase difference between these two TE_0 modes propagating in the two MZI arms. Therefore, one can freely achieve a controllable $TE_0 - TM_0$ mode conversion by utilizing such a special polarization converter. Meanwhile, PS #1 and PS #3 are inserted, respectively, to tune the phase difference between the TE_0 and TM_0 modes in the input/output sections as required. When light with an arbitrary SOP is launched into the chip, the TE_0 and TM_0 modes in the silicon photonic waveguide are excited, respectively. The TE_0 mode passes through PS #1 and PDMC #1 almost losslessly, while the TM_0 mode is efficiently converted to the TE_1 mode by PDMC #1. Meanwhile, the TE_0 and TE_1 modes have some phase differences δ, depending on the waveguide birefringence and the thermal tuning of PS #1 (introducing a phase delay φ_1). As a result, mode interference occurs when the TE_0 and TE_1 modes pass through the DMPS #1 simultaneously, and the power ratio and the phase difference of the two split TE_0 modes are determined by that of the TE_0 and TE_1 modes. These two TE_0 modes enter the MZI arms (arm #1 and arm #2), and their phase difference is further tuned by PS #2 (with an addition of φ_2). After passing through DMPS #2, one can acquire the TE_0 and TE_1 modes with an adjustable power ratio and phase difference. Then the TE_1 mode is converted to the TM_0 mode, while the TE_0 mode is kept unchanged by using PDMC #2. Finally, the phase difference of the TE_0 and TM_0 modes at the output port can flexibly be tuned as desired by tuning PS #3 to generate any SOP in the output fiber or the free space. With the transmission matrix of the whole chip, the output field $[E'_x, E'_y]^T$ (defined by the amplitudes $[a'_x, a'_y]$ and the phase difference δ') is related to the input field $[E_x, E_y]^T$ (defined by the amplitudes $[a_x, a_y]$ and the phase difference δ_0) with the following equation:

$$\begin{bmatrix} E'_x \\ E'_y \end{bmatrix} = C_{P3} C_{PC} C_{P1} \begin{bmatrix} E_x \\ E_y \end{bmatrix}, \quad (2)$$

in which C_{P1}, C_{PC}, and C_{P3} are the transmission matrices of PS #1, the polarization converter, and PS #3. They are given as

$$C_{P1} = \begin{bmatrix} 1 & 0 \\ 0 & e^{-i(\varphi_1+\delta_1)} \end{bmatrix}, \quad (3)$$

$$C_{PC} = \frac{1}{2} \begin{bmatrix} 1 + e^{-i\varphi_2} & -e^{-\frac{\delta_2}{2}} + e^{-i(\varphi_2+\frac{\delta_2}{2})} \\ -e^{-\frac{\delta_2}{2}} + e^{-i(\varphi_2+\frac{\delta_2}{2})} & e^{-i\delta_2} + e^{-i(\varphi_2+\delta_2)} \end{bmatrix}, \quad (4)$$

$$C_{P3} = \begin{bmatrix} 1 & 0 \\ 0 & e^{-i(\varphi_3+\delta_3)} \end{bmatrix}, \quad (5)$$

where φ_1, φ_2, and φ_3 are, respectively, the phase changes induced by the parts of PS #1, the polarization converter, and PS #3; δ_1, δ_2, and δ_3 are the phase differences induced by the waveguide birefringence in these three parts.

With the transmission matrix given above, the performance of the proposed PC can be evaluated clearly. For the sake of simplicity, we set $\delta_{1,2,3}$ to be 0 in the following discussion. When the x-polarized light (i.e., the TE_0 mode) or y-polarized light (i.e., the TM_0 mode) is launched, the PER can be tuned by adjusting PS #2 only (depending on the phase shifting φ_2). Here we consider the case with the TE_0 mode (which has $[a_x^2, a_y^2, \delta_0] = [1, 0, 0]$) as an example. Figure 2(a) shows the normalized results of a_x^2 and a_y^2 for the output field as the phase shifting φ_2 varies from 0 to 2π. It can be seen that arbitrary a_x^2 and a_y^2 can be achieved in the range of [0,1]. Figure 2(b) shows the calculated phase difference δ' for the output field when the phase-shifting φ_3 is 0, having two discrete values of 1.5π and 0.5π. When tuning the phase-shifting φ_3, arbitrary phase difference δ' can also be achieved for the output field. As a result, one can traverse the Poincaré sphere as the phase-shiftings φ_2 and φ_3 are tuned in the range of $[0, 2\pi]$, as shown in Fig. 2(c). Here the SOP is described with normalized Stokes parameters, i.e., S_1, S_2, and S_3, which are defined as

$$\begin{cases} S_1 = a_x^2 - a_y^2 \\ S_2 = 2a_x a_y \cos \delta. \\ S_3 = 2a_x a_y \sin \delta \end{cases} \quad (6)$$

Another example considered here is the case when the input light is 45°-polarized (i.e., $[a_x^2, a_y^2, \delta_0] = [1/2, 1/2, 0]$). Figures 2(d) and 2(e) show the calculated results of the normalized power a_x^2 and a_y^2, and the phase difference for the output field as the phase shifting φ_2 varies from 0 to 2π. Here the phase-shifting φ_1 is assumed to be 0, 0.2π, or 0.5π. When $\varphi_1 = 0$, one always has $a_x'^2 = a_y'^2 = 1/2$ and $\delta' = 0$, which is independent of the phase-shifting φ_2, indicating the polarization converter is unable to tune the light SOP. When choosing $\varphi_1 = 0.2\pi$, the normalized power can be tuned in the range of [0.2, 0.8] and it is still unable to achieve an arbitrary power range of [0,1]. Instead, when choosing $\varphi_1 = \pi/2$, a normalized power range of [0,1] can be achieved, as shown in Fig. 2(d). The corresponding phase difference δ' is shown in Fig. 2(e). As a result, for the 45°-polarized input light, one can traverse the Poincaré sphere by fixing $\varphi_1 = 0.5\pi$ and scanning φ_2 and φ_3 in the range of $[0, 2\pi]$, as shown in Fig. 2(f).

According to the transmission matrix given in Eq. (2), the phase difference between the TE_0 and TM_0 modes should be chosen as $\delta = \delta_0 + \delta_1 + \varphi_1 = 2\pi \pm 0.5\pi$, thus making sure that a_x^2 and a_y^2 can be tuned from 0 to 1. For example, for the launched light beam with $[a_x^2, a_y^2, \delta_0] = [0.25, 0.75, 0.25\pi]$, Figs. 2(g) and 2(h) show the calculated normalized power $a_x'^2$ and $a_y'^2$ and the phase difference δ' for the output field as the phase-shifting φ_2 varies from 0 to 2π. Here the phase-shifting φ_1 is assumed to be 0.25π, 0.75π, and 1.25π. It can be seen that $a_x'^2$ and $a_y'^2$ can cover the range of [0,1] by tuning φ_2 when φ_1 is set to be 0.25π or 1.25π, while for $\varphi_1 = 0.75\pi$, the tuning range covers [0.25, 0.75] only. The calculated corresponding δ' is shown in Fig. 2(h). By fixing $\varphi_1 = 0.25\pi$ or 1.25π, and scanning φ_2 and φ_3 in the range of $[0, 2\pi]$, one can also traverse the Poincaré sphere for the launched light beam $[a_x^2, a_y^2, \delta_0] = [0.25, 0.75, 0.25\pi]$, as shown in Fig. 2(i).
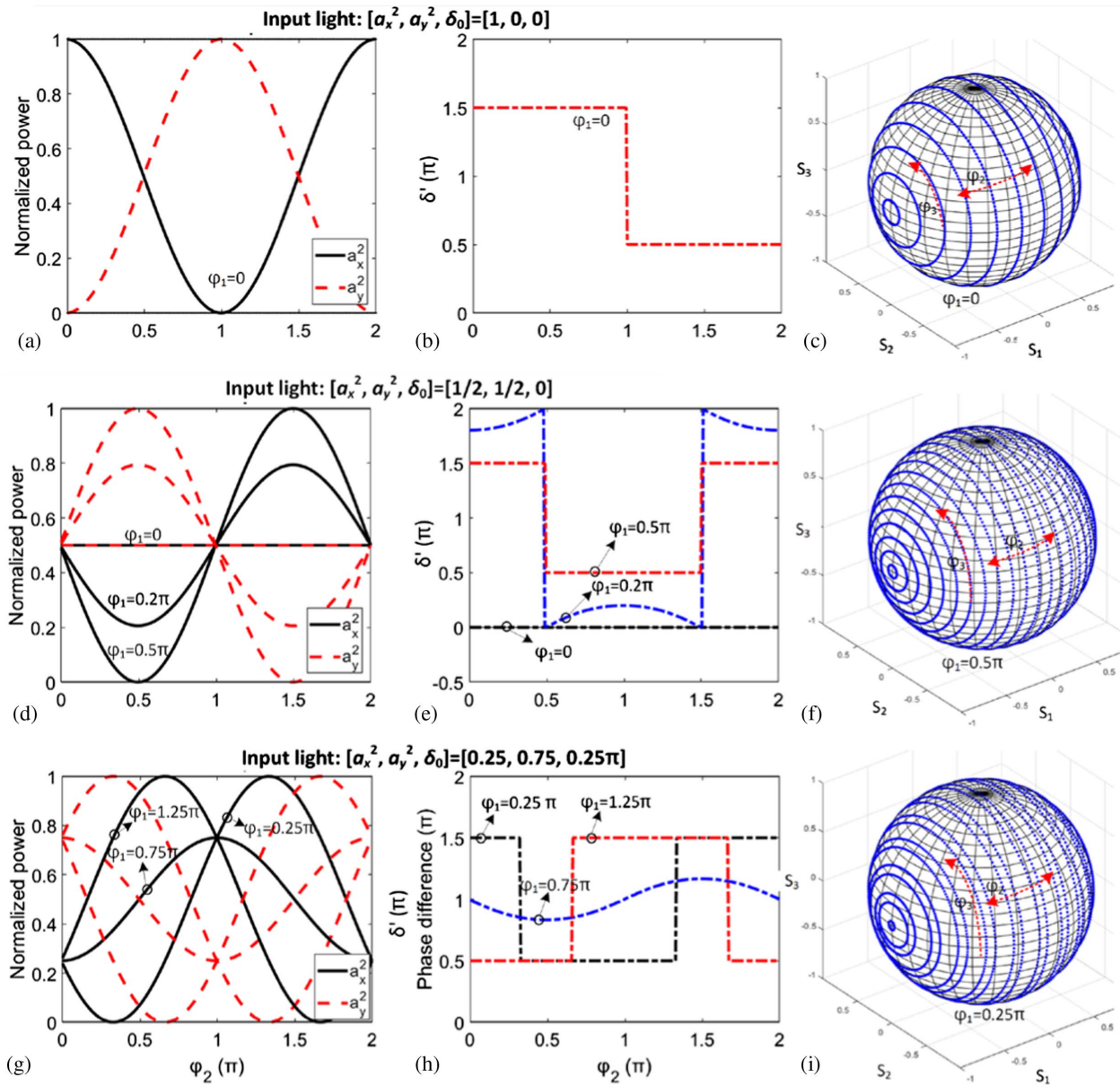
Fig. 2. Calculated output transmissions $[a_x'^2, a_y'^2, \delta']$ for the launched light with different $[a_x^2, a_y^2, \delta_0]$. (a), (d), (g) show the normalized power $a_x'^2$ and $a_y'^2$; (b), (e), (h) show the phase difference δ'; (c), (f), (i) show recorded Poincaré sphere when scanning φ_2 and φ_3. Here, one chooses $[a_x^2, a_y^2, \delta_0] = [1, 0, 0]$ for (a)–(c), $[a_x^2, a_y^2, \delta_0] = [1/2, 1/2, 0]$ for (d)–(f), $[a_x^2, a_y^2, \delta_0] = [1/4, 3/4, \pi/4]$ for (g)–(i), respectively.

In order to realize the on-chip PC, here we use an SOI wafer with a 220-nm-thick top silicon core layer (i.e., $h_c = 220$ nm) and a 2-μm-thick buried oxide layer (i.e., $h_b = 2$ μm). Figure 1(b) shows the cross section of the fully etched silicon photonic waveguide, which has a silica upper cladding with a thickness of $h_{cl} = 2.2$ μm and a 300-nm-thick Cr/Au heater embedded in the upper cladding. The simulated field profiles of the TE_0 and TM_0 modes in a 400-nm-wide silicon photonic waveguide are given in Fig. 3(a) as an example, showing that the TE_0 mode is more confined in the silicon core than the TM_0 mode when $w_{co} > 220$ nm. As a result, it is expected that the TE_0 mode has a higher effective thermo-optic coefficient dN_{eff}/dT than the TM_0 mode because silicon has a much more significant thermo-optical coefficient than silica.

Figure 3(b) shows the calculated results for the effective thermo-optic coefficients dN_{eff}/dT of the TE_0 and TM_0 modes. It can be seen that the coefficient dN_{eff}/dT of the TE_0 mode increases from $\sim 1.43 \times 10^{-4}/°C$ to the maximum of $\sim 1.93 \times 10^{-4}/°C$ and then decreases to $\sim 1.82 \times 10^{-4}/°C$ eventually as the core width increases from 0.3 to 1.2 μm. In contrast, the coefficient dN_{eff}/dT of the TM_0 mode increases monotonously from $\sim 0.61 \times 10^{-4}/°C$ to the maximum of $\sim 1.35 \times 10^{-4}/°C$. Accordingly, the difference between the coefficients dN_{eff}/dT of the TE_0 and TM_0 modes is also given in Fig. 3(b), showing that there is a maximum of $\sim 1.02 \times 10^{-4}/°C$ achieved for the optimized core width $w_{co} = 0.35$ μm. With this design, the power consumption of PS #1 and PS #3 can be minimized for achieving the target
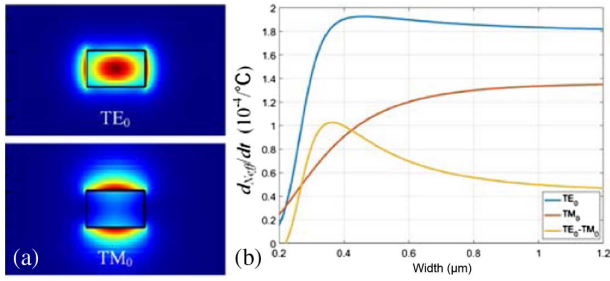
Fig. 3. (a) Simulated TE_0 and TM_0 mode field profiles of the fully etched silicon photonic waveguide; (b) calculated effective thermo-optic coefficients dN_{eff}/dT for the TE_0 and TM_0 modes, and the difference between their thermo-optic coefficients.

phase difference δ. On the other hand, the propagation loss for 0.35-μm-wide silicon photonic waveguides is usually high due to the scattering at the waveguide sidewalls [43]. Therefore, in this paper we choose the core width as $w_{co} = 0.4$ μm (slightly wider than the optimal value 0.35 μm) for the sections of PS #1 and PS #3 for balancing between the propagation loss and the power consumption. In this case, the coefficients dN_{eff}/dT of the TE_0 and TM_0 modes have a difference $\Delta(dN_{eff}/dT)$ of about $1.0 \times 10^{-4}/°C$, which is slightly lower than the maximum of $1.02 \times 10^{-4}/°C$ at $w_{co} = 0.35$ μm. Accordingly, the maximal temperature increase is approximately 155°C to achieve a phase difference of 2π when the length of the heating section is chosen as 100 μm. Therefore, in this paper we choose the lengths of PS #1 and PS #3 to be 100 μm for compact footprints as well as a moderate heating temperature.

The PDMCs are designed by utilizing the mode hybridity in a bilevel waveguide taper, enabling the mode conversion from a fully etched strip waveguide to a shallowly etched ridge waveguide, as shown in Fig. 4(a). In this paper, the slab thickness for the ridge waveguide is chosen to be $h_s = 70$ nm for implementing the desired mode hybridity and accommodating the standard foundry process as shown in Fig. 1(c). Figure 4(a) shows the calculated effective indices of the TE_0, TM_0, and TE_1 modes of the bilevel ridge waveguide as the core width varies from 0.4 to 0.8 μm. It can be seen that there is a region around $w_{co} = 0.53$ μm where the TM_0 – TE_1 mode hybridity occurs. As a result, when the PDMC is designed by using an adiabatic bilevel taper with a core width gradually varying from 0.4 to 0.8 μm, the launched TM_0 mode can be converted to the
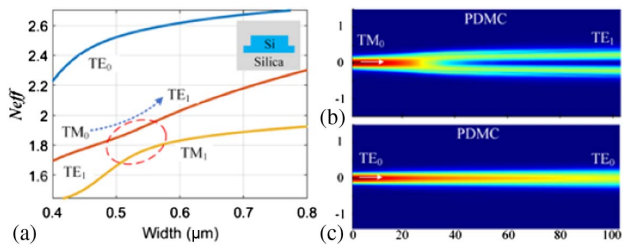

Fig. 4. (a) Calculated effective indices of the TE_0, TM_0, and TE_1 modes of the bilevel ridge waveguide as the core width varies. Simulated light propagation in the designed PDMC when the (b) TM_0 mode and the (c) TE_0 mode are launched.

TE_1 mode efficiently, as shown in Fig. 4(b), which is due to the mode hybridity [41]. In contrast, the TE_0 mode passes through the PDMC losslessly, as shown in Fig. 4(c). Here the PDMC and DMPSs are designed with the parameters given in Ref. [41].

Figure 5(a) shows the simulated light propagation in the structure consisting of PS #1, PDMC #1, and DMPS #1 when the TE_0 mode is launched as an example. It can be seen that the TE_0 mode goes through PS #1 and PDMC #1 losslessly. Then it is split symmetrically and coupled to the two TE_0 modes of two MZI arms by DMPS #1. In contrast, the launched TM_0 mode is converted to the TE_1 mode by PDMC #1 due to the mode hybridity. The TM_1 mode is then split and coupled to the TE_0 modes of the two MZI arms, which have a power ratio of 50%:50% and a phase difference of π, as shown in Fig. 5(b). Note that PS #1 does not introduce any modification to the light SOP for the TE_0 or TM_0 mode launched alone. Otherwise, for the light SOP with the TE_0 and TM_0 modes excited simultaneously, PS #1 plays a key role for the polarization conversion, as discussed earlier. For example, for the 45°-polarized light launched into the chip, the TE_0 and TM_0 modes are excited with equal power and zero phase difference, and the TM_0 mode is further converted into the TE_1 mode [see Fig. 5(b)]. In this case, the interference between the TE_0 mode and the TE_1 mode occurs, which depends on the phase difference δ between them. The TE_0 – TE_1 mode interference finally determines the power splitting ratio of the DMPS for the TE_0 modes in the MZI arms, indicating that the splitting ratio of DMPS #1 can be adjusted freely by tuning the phase-shifting φ_1 of PS #1. For example, when phase difference $\delta = 0$, the power-splitting ratio of the DMPS is 0:100% and light is fully coupled to the TE_0 mode in the upper MZI arm when operating at 1550 nm, as shown in Fig. 5(c). When $\delta = \pi$, the power-splitting ratio of the DMPS is 100%: 0 and light is fully coupled to the TE_0 mode in the lower MZI arm, as shown in Fig. 5(d). When $\delta = 2m\pi \pm \pi/2$, the power-splitting ratio of the DMPS is about 50%:50%, as shown in Fig. 5(e). Similarly, it is always possible to achieve a power-splitting ratio of 50%:50% for any light SOP by tuning the phase-shifting δ. Note that the power-splitting ratio of 50%:50% is the key to achieving arbitrary SOP for the emitted light.

As a key role, PS #2 is used to tune the phase difference φ_2 between the TE_0 modes propagating along the two MZI arms, enabling the adjustment of the power ratio of the TE_0 and TE_1 modes at the output port of DMPS #2. The TE_1 mode is then converted completely to the TM_0 mode after going through PDMC #2. As a result, PS #2 actually plays the role of tuning the PER of the TE_0 and TM_0 modes at the output port. Figure 6 shows the simulated light propagation in the structure consisting of two MZI arms, DMPS #2, and PDMC #2. Here two TE_0 modes with an initial phase difference of $\delta_0 = 0$ are launched into the two MZI arms. When $\varphi_2 = 0$, these two TE_0 modes finally are recombined and coupled to the TE_0 mode at the output end of DMPS #2. Then the TE_0 mode goes through PDMC #2 losslessly, as shown in Fig. 6(a). In contrast, when $\varphi_2 = \pi$, these two TE_0 modes in the two MZI arms are combined to be the TE_1 mode after passing DMPS #2, and finally the TE_1 mode is converted to the
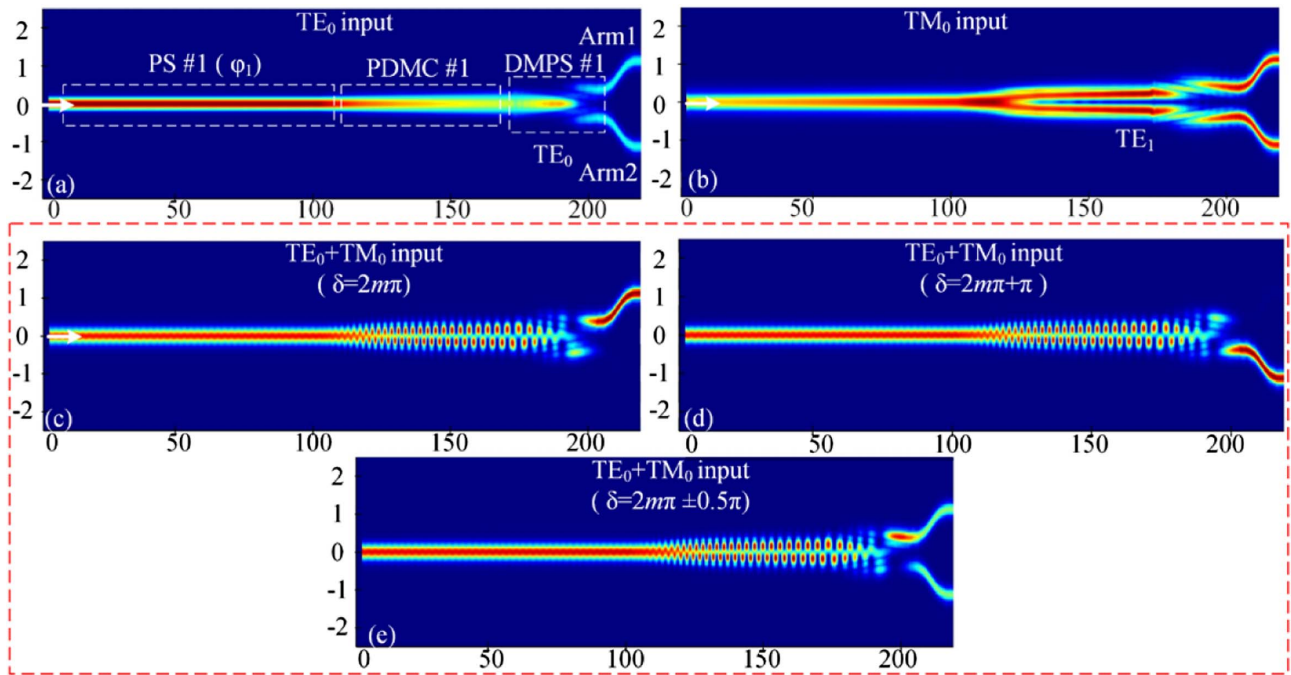
Fig. 5. Light propagation at the regions of PS #1, PDMC1, and DMPS #1 for (a) the TE_0 mode, (b) the TM_0 mode, and the 45° linearly polarized light under different δ; (c) $\delta = 2m\pi$; (d) $\delta = 2m\pi + \pi$; (e) $\delta = 2m\pi \pm 0.5\pi$ (at 1550 nm).
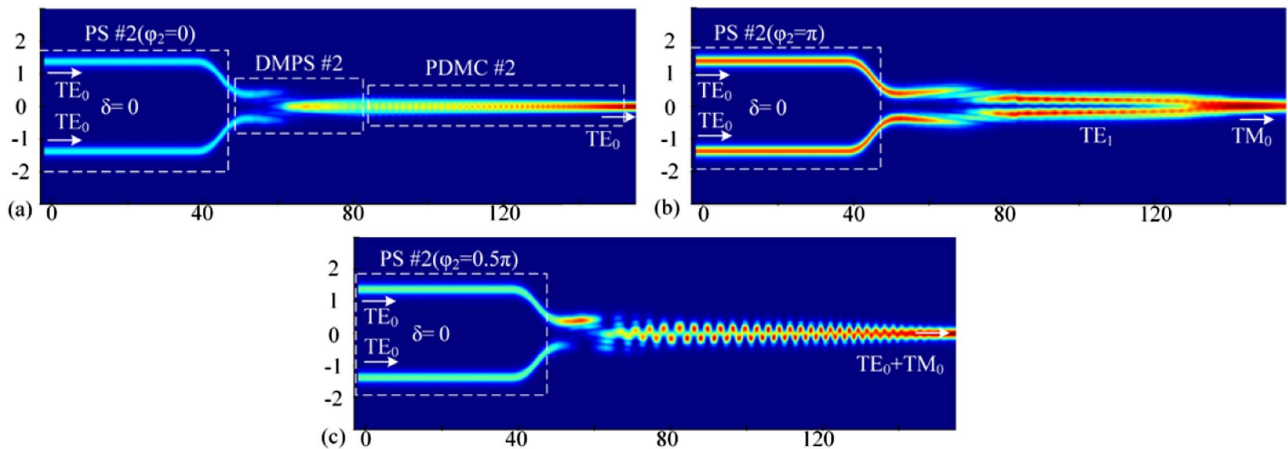
Fig. 6. Light propagation for the two TE_0 modes launched into the two arms of the MZI, when (a) $\varphi_2 = 0$; (b) $\varphi_2 = \pi$; (c) $\varphi_2 = 0.5\pi$.

TM_0 mode at the output port by PDMC #2, as shown in Fig. 6(b). Figure 6(c) also shows the light propagation for the $\varphi_2 = 0.5\pi$; the output TE_0 and TM_0 modes have a power ratio of 50%:50%.

3. FABRICATION AND MEASUREMENT

The chip was fabricated with the standard 220-nm-thick SOI foundry process, and a two-step etching process was used to form the bilayer ridge waveguides. Figures 7(a) and 7(b) show the optical micrographs of the fabricated chip and the polarization converter, and Fig. 7(c) shows the scanning electron micrograph (SEM) of the DMPS. The fabricated
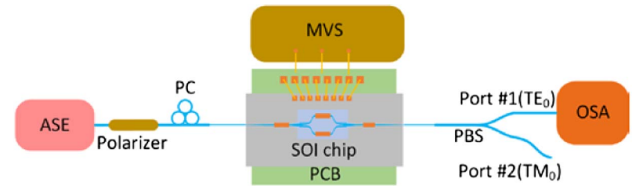
chip was diced and polished for efficient fiber-chip edge coupling.

The fabricated PC was first measured using the experimental setup shown in Fig. 8. Light from the amplified spontaneous emission (ASE) source passes through a fiber inline polarizer and a fiber PC (PC) and finally enters the chip through the edge coupler. At the output side, the TE_0 mode (Port #1) and the TM_0 mode (Port #2) of the emitted light are separated with a fiber polarization beam splitter (PBS) and received by an optical spectrum analyzer (OSA). The three PSs are thermally tuned by injecting the currents to the corresponding microheaters connected with a multichannel voltage source (MVS) via a printed circuit board (PCB).
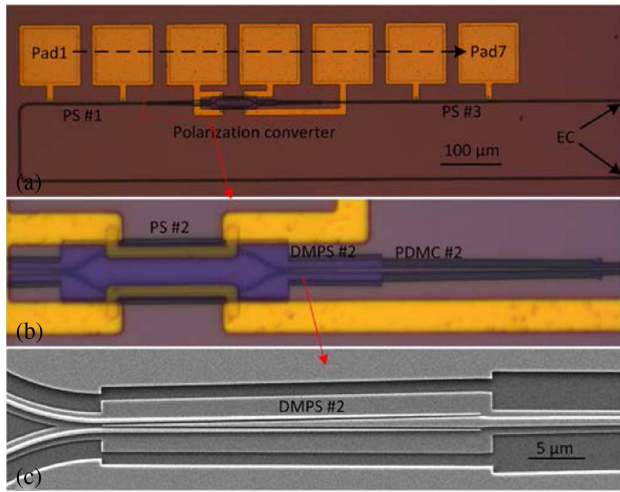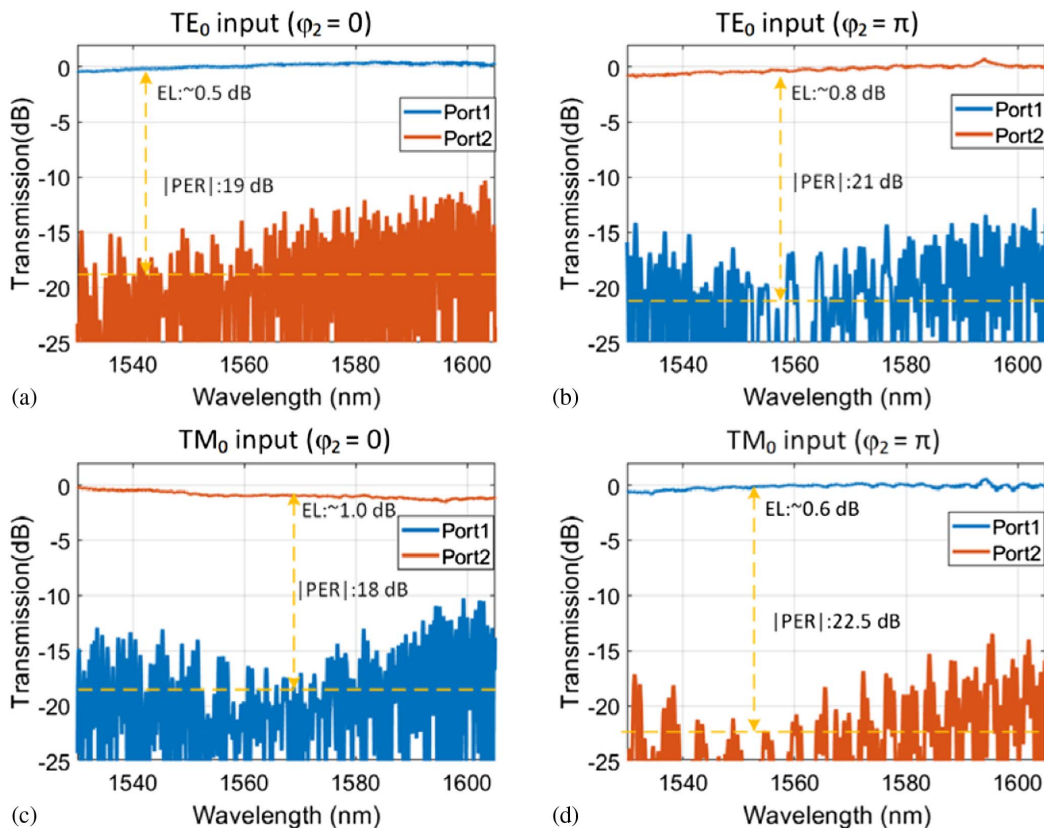
Fig. 7. (a) Optical micrographs of the fabricated PC; (b) enlarged view for the polarization converter; (c) SEM of the DMPS.


Fig. 8. Experiment setup for characterizing the polarization converter. ASE, amplified spontaneous emission; PC, fiber polarization controller; MVS, multichannel voltage source; PBS, fiber polarization beam splitter; OSA, optical spectrum analyzer.

TE_0 mode has an EL less than 0.5 dB (blue line) and PER larger than 12 dB in the 1530–1605 nm wavelength range, and the largest PER is about 19 dB at 1542 nm wavelength. When PS #2 is on ($P_2 = 18.7$ mW, $\varphi_2 = \pi$), the $TE_0 – TM_0$ mode conversion happens; the outputs of Port #1 and Port #2 are shown in Fig. 9(b). The $TE_0 – TM_0$ conversion has an EL of ~0.8 dB and a PER larger than 15 dB at 1530–1605 nm, and the largest PER is ~21 dB at 1558 nm. The measured transmissions for the launched TM_0 mode are shown in Figs. 9(c) and 9(d). When PS #2 is off, the TM_0 mode has an on-chip EL less than ~1 dB and a PER larger than 12 dB in the spectral range of 1530–1605 nm, and the largest PER of 18 dB is achieved at 1568 nm. While PS #2 is on with a power of 18.7 mW, the $TM_0 – TE_0$ conversion has an EL ~0.6 dB and a PER larger than 15 dB in the spectral range

Figures 9(a)–9(d) show the measured spectra from output Port #1 and Port #2 when the TE_0 or TM_0 modes are selectively excited by controlling fiber PC from the input side. Here the results are normalized, with the spectrum of a straight waveguide fabricated on the same chip. The measured transmissions for the launched TE_0 mode when PS #2 is at the off state ($P_2 = 0$ mW, $\varphi_2 = 0$) are shown in Fig. 9(a). The

Fig. 9. Measured transmissions at Port #1 and Port #2 of the PC when the (a), (b) TE_0 and (c), (d) TM_0 modes are, respectively, input; (a), (c) $\varphi_2 = 0$; (b), (d) $\varphi_2 = \pi$.
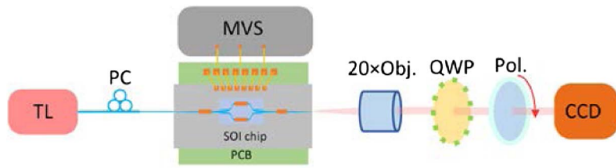
Fig. 10. Experiment setup for observing the output mode field. TL, tunable laser; PC, polarization controller; MVS, multichannel voltage source; QWP, quarter-wave plate; Pol., polarizer; CCD, charge coupled device.

of 1530–1605 nm, and one has the largest PER of 22.5 dB at 1552 nm. As a result, the attainable PER range is >40 dB for both TE_0 and TM_0 modes. It should be mentioned that the measured device PER range is limited by the fiber PBS used, which has a PER of 20 dB.

Figure 10 shows the experiment setup to demonstrate the generation of arbitrary SOPs for 1550 nm by using the present chip. Light from a tunable laser (TL) passes through a fiber PC and then is coupled to the chip. Light from the output port of the chip is collected through a 20× objective lens and finally is captured by using a charge coupled device (CCD). Here a quarter-wave plate (QWP) and a polarizer were used to test the SOP of the output light.

Figure 11(a) shows the captured free-space mode field profiles when the TE_0 mode is launched. Here the phase difference φ_2 introduced by PS #2 is tuned to be 0 or π. When setting $\varphi_2 = 0$, a fundamental mode field profile is observed clearly by aligning the polarizer to be parallel to the x axis. Otherwise, when aligning the polarizer to be vertical to the x axis, nothing is observed. This indicates that the light emitted from the chip is the TE_0

mode when $\varphi_2 = 0$. In contrast, when setting $\varphi_2 = \pi$, a fundamental mode field profile is observed clearly by aligning the polarizer to be vertical to the x axis, indicating that the light SOP is converted successfully from the TE_0 mode launched at the input port to the TM_0 mode emitted at the output port, as shown in Fig. 11(a). Similarly, the TM_0 mode launched from the input port can also be converted to the TE_0 mode or be kept as the TM_0 mode, depending on the phase difference φ_2, as shown in Fig. 11(b).

The launched mode can be further converted to the circularly polarized light beam by adjusting the phase difference φ_2. When $\varphi_2 = \pi/2$, the launched TE_0 mode can be converted equally to the TE_0 and TM_0 modes with the same powers by the polarization converter. Then the phase difference δ between the TE_0 and TM_0 modes can be set as $2m \pm 0.5\pi$ by tuning the heating power of PS #3 elaborately. As a result, the mode field pattern observed by the camera did not change, as the polarizer is rotated without a QWP [see the upper portion of Fig. 11(c)]. When a QWP is further inserted between the lens and the polarizer, the circularly polarized light is converted to the linearly polarized light, and thus the SOP can be characterized easily and clearly by the polarizer, as shown at the bottom of Fig. 11(c). The maximum transmittance is achieved when the axis of the polarizer is rotated to 45° or 195°, and the minimum transmittance is achieved when the axis of the polarizer is rotated to 135° or 315°.

To further demonstrate the generation of the arbitrary SOP by using the present PC, a polarimeter (PAX1000IR2) working at the 1550 nm wavelength band was used to characterize the SOP of the light beam generated at the output port. Figures 12(a) and 12(b) show the recorded SOP plotted on the Poincaré sphere for the launched TE_0 and TM_0 modes.
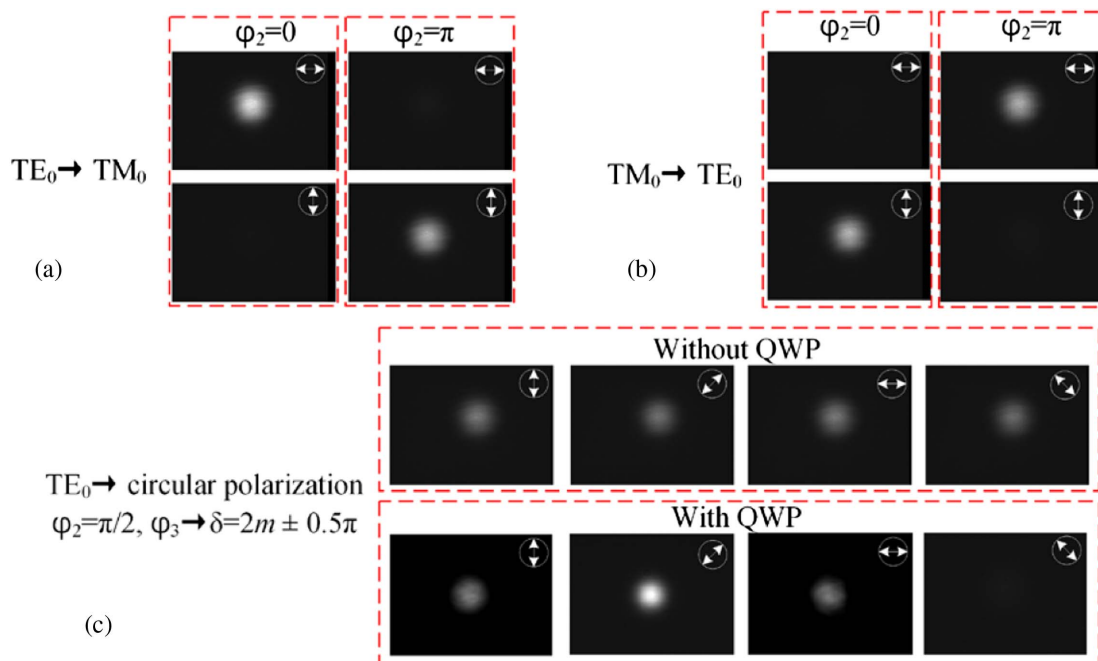
Fig. 11. Captured output mode field for the generated SOP at 1550 nm. (a) TM_0 mode generation from the launched TE_0 mode; (b) TE_0 mode generation from the launched TM_0 mode; (c) circularly polarized light generation from the launched TE_0 mode. The arrows indicate the axis of the polarizer.
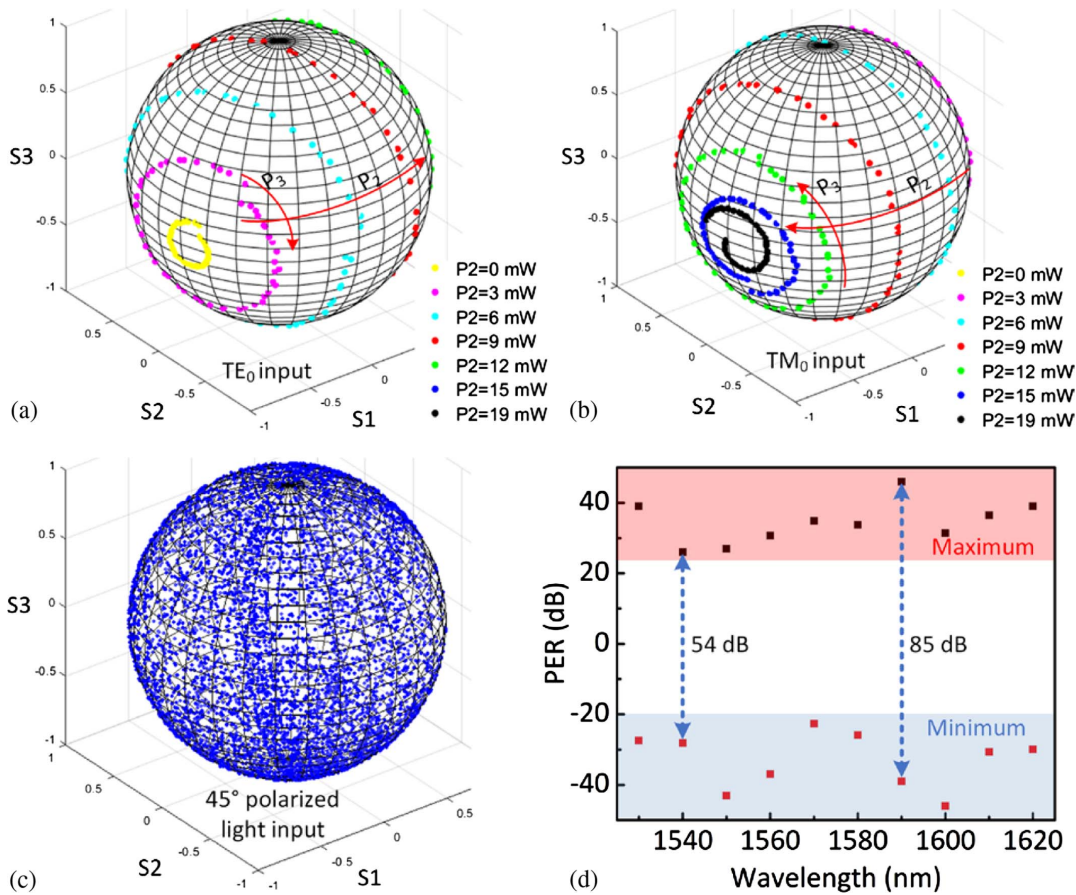
Fig. 12. Measured SOP on the Poincaré sphere for (a) the input TE_0 mode, (b) the input TM_0 mode, and (c) a $\sim$45° linearly polarized light beam. In (a) and (b), P_2 was fixed at different steps, and for each P_2, a sweep of the P_3 was performed. In (c), the P_1, P_2, and P_3 were swept simultaneously, thus producing $\sim$6000 points traversing the entire Poincaré sphere. (d) The measured PER range for the launched TE_0 mode operating with different wavelengths.

Here the SOP is described with normalized Stokes parameters, i.e., S_1, S_2, and S_3. For the input TE_0 mode, as shown in Fig. 12(a), PS #2 was tuned with different powers to make the PER vary from $-\infty$ to ∞. Meanwhile, for any given power P_2 applied to PS #2, the power P_3 applied to PS #3 was scanned from 0 to 25 mW with a step of $\sim$0.4 mW, so that the phase difference between the TE_0 and TM_0 modes is swept from 0 to 2π. The power P_3 sweeping traces the parallel circular orbits on the Poincaré sphere, while the step size of the power P_2 defines the spacing between adjacent orbits. The measured results have a good correspondence with the simulation result shown in Fig. 2. Theoretically, when $P_2 = 0$, the TE_0 mode with a high PER is generated, it corresponds to the point $[S_1, S_2, S_3] = [-1, 0, 0]$ on the Poincaré sphere, while the SOP is kept unchanged when scanning the power P_3. Note that the SOP of the emitted light changes in some degree due to the propagation in the output fiber; moreover, the heating-induced thermal cross talk also breaks the SOP to a certain extent. As a result, the measured SOP traced a small circular orbit, as shown in Fig. 12(a), and the swept point $[S_1, S_2, S_3] = [-0.99, -0.13, -0.04]$ has the maximal negative PER of $\sim$$-23$ dB, indicating a TE_0 mode with high PER is generated.

Meanwhile, at the far side of the Poincaré sphere, point $[S_1, S_2, S_3] = [1, 0.05, 0]$ achieves the maximal positive PER of $\sim$32 dB for the case of $P_2 = 19$ mW, indicating a complete conversion from the TE_0 mode to the TM_0 mode. Similar phenomena are observed for the case with the input TM_0 mode, as shown in Fig. 12(b). Two nearly perfect points $[S_1, S_2, S_3] = [-1, 0, -0.02]$ (with PER $= -34$ dB), $[S_1, S_2, S_3] = [1, -0.03, -0.03]$ (with PER $= 33$ dB, at the far side of the Poincaré sphere) are achieved. In general, the record PER tuning range is 55 and 67 dB for the launched TE_0 and TM_0 modes, respectively.

For the present structure, any SOP can be generated easily from the input TE_0 or TM_0 modes by controlling the phase shifting of PS #2 and PS #3. In contrast, when an elliptically polarized light beam is input, the phase shifting of PS #1 should also be adjusted carefully to make sure the phase difference $\delta = 2\pi \pm 0.5\pi$, and hence one can traverse the entire Poincaré sphere. For example, the input light is set to be $\sim$45° linearly polarized, and the feeding powers of PS #1, PS #2, and PS #3 are simultaneously swept from 0 to 40 mW with 18 steps. The $\sim$6000 points recorded by the polarimeter can fully cover the entire surface of Poincaré sphere

Table 1.   Performance Metrics Comparison of the Representative PCs

Refs.	Architecture	Platform	Power (mW) or V_π (V)	PER Range (dB)	Length (μm)	EL (dB)	Working Bandwidth (nm)
[25]	2PSR + 5MZI	SOI + SiN	40 mW	~	~2500	<4.5	At 1550 nm
[26]	2D grating + 6 MZI	SOI	27 mW	36	~	6.5	At 1550 nm
[27]	2PSR + 3MZI	LN	2.4 V	41.9	45,000	0.92	At 1550 nm
[30]	3PR + 3PS	SOI	~300–700 mW	40	~3000	<3	40
This work	**1 Polarization converter + 2 PS**	**SOI**	**25 mW**	**54–85**	**700**	**<1**	**90**

benefiting from the device's larger PER range, as shown in Fig. 12(c), proving that one can convert two arbitrary SOPs with the proposed PC. The proposed PC is intrinsically narrow in bandwidth due to the high birefringence of silicon photonic waveguides [30]. Here a large PER range can be achieved in a wide bandwidth by appropriately applying the control power to the PC optimized for different wavelengths. Figure 12(d) shows the measured PER range for the launched TE_0 mode when operating with different wavelengths. Here the powers P_2 and P_3 are swept to produce ~1000 points on the Poincaré sphere, and the points with the maximized PER are recorded in Fig. 12(d), showing that the PC has a high PER range of 54–85 dB in the wavelength range of 1530–1620 nm.

Table 1 shows the summary of the representative PCs reported. Currently, there are mainly two routes for the realization of on-chip polarization management. One is using the combination of PSRs and a 2×2 MZI [25–27], while the other is using the combination of polarization rotators and phase shifters [30]. Theoretically, to achieve arbitrary SOP conversion, one has to introduce two PSRs, three MZIs, and two MMIs. However, the imperfection performances of the PSRs and the MMIs mean it has a limited PER range of less than 23 dB; thus, it is difficult to traverse the Poincaré sphere as demonstrated in Ref. [27]. Usually, the multistage design has to be introduced to increase the PER as desired [25,27]. Although a PER of 41 dB can be achieved, the total length is larger than 4.5 cm, and the devices' behavioral predictability also decreases prominently. In comparison, our scheme contains a polarization converter and two PSs and has an ultracompact layout footprint. The critical PDMC works on the principle of mode hybridity and mode evolution of an adiabatically tapered ridge waveguide [42,44]. Meanwhile, the DMPS based on a tapered trident waveguide also works adiabatically [45]. As is well known, adiabatic tapers usually work with a broad bandwidth and large fabrication tolerances. Moreover, the structure symmetry of the DMPS is helpful to ensure the power-splitting ratio of 50%:50% for both TE_0 and TE_1 modes, as desired. Therefore, our scheme has an ultracompact and robust framework, featuring comprehensive advantages in the device footprint, the PER, the bandwidth, and the EL. As a result, our scheme has an ultracompact, robust framework, and features comprehensive advantages in footprint, PER, bandwidth, and EL.

4. CONCLUSION

In conclusion, we have proposed and demonstrated a novel PC by forming two phase shifters on a high-performance polarization converter's input/output waveguide. For the input light

beam with arbitrary SOP, its E_x and E_y components excite the TE_0 and TM_0 modes, respectively. The PS #1 and polarization converter reallocate the PER of the TE_0 and TM_0 modes, while PS #3 tunes their phase difference. Thus, one can achieve the conversion of two arbitrary SOPs. The proposed PC works on the adiabatic mode evolution principle and is the structure of perfect symmetry, thus having larger fabrication tolerance. As a result, our scheme is ultracompact and robust and shows comprehensive advantages in footprint, PER, and EL. The fabricated PC has a compact layout footprint of ~150 μm × 700 μm, an EL of less than 1 dB, and a record PER range of >54 dB in the wavelength range of 1530–1620 nm. One can convert two arbitrary SOPs with the proposed PC by feeding the PSs #1–3 with suitable power. Such a compact, high-performance polarization management device could be vital in many applications.

Disclosures.   The authors declare no conflicts of interest.

Data Availability.   Data underlying the results presented in this paper are not publicly available at this time but may be obtained from the authors upon reasonable request.

REFERENCES

1. R. Noe, B. Koch, V. Mirvoda, *et al.*, "38-krad/s 3.8-Grad broadband endless optical polarization tracking using LiNbO₃ device," IEEE Photon. Technol. Lett. **21**, 1220–1222 (2009).
2. B. Koch, R. Noe, D. Sandel, *et al.*, "20-Gb/s PDM-RZ-DPSK transmission with 40 krad/s endless optical polarization tracking," IEEE Photon. Technol. Lett. **25**, 798–801 (2013).
3. M. Yamanari, Y. Lim, S. Makita, *et al.*, "Visualization of phase retardation of deep posterior eye by polarization-sensitive swept-source optical coherence tomography with 1-μm probe," Opt. Express **17**, 12385–12396 (2009).
4. B. Kunnen, C. Macdonald, A. Doronin, *et al.*, "Application of circularly polarized light for non-invasive diagnosis of cancerous tissues and turbid tissue-like scattering media," J. Biophoton. **8**, 317–323 (2015).
5. Y. M. Noh, D. Müller, H. Lee, *et al.*, "Influence of biogenic pollen on optical properties of atmospheric aerosols observed by lidar over Gwangju, South Korea," Atmos. Environ. **69**, 139–147 (2013).
6. N. Hu, Y. Meng, K. Zou, *et al.*, "Full-Stokes polarimetric measurements and imaging using a fractal superconducting nanowire single-photon detector," Optica **9**, 346–351 (2022).

7. M. Losurdo, M. Bergmair, G. Bruno, *et al.*, "Spectroscopic ellipsometry and polarimetry for materials and systems analysis at the nanometer scale: state-of-the-art, potential, and perspectives," J. Nanopart. Res. **11**, 1521–1554 (2009).

8. J. Y. Cho, J. H. Lim, and K. S. Lee, "Optical fiber twist sensor with two orthogonally oriented mechanically induced long-period grating sections," IEEE Photon. Technol. Lett. **17**, 453–455 (2005).

9. A. M. Smith, "Birefringence induced by bends and twists in single-mode optical fiber," Appl. Opt. **19**, 2606–2611 (1980).

10. B. J. Shastri, A. N. Tait, T. Ferreira de Lima, *et al.*, "Photonics for artificial intelligence and neuromorphic computing," Nat. Photonics **15**, 102–114 (2021).

11. A. H. Atabaki, S. Moazeni, F. Pavanello, *et al.*, "Integrating photonics with silicon nanoelectronics for the next generation of systems on a chip," Nature **556**, 349–354 (2018).

12. G. Chen, N. Li, J. D. Ng, *et al.*, "Advances in lithium niobate photonics: development status and perspectives," Adv. Photon. **4**, 034003 (2022).

13. D. Dai, "Advanced passive silicon photonic devices with asymmetric waveguide structures," Proc. IEEE **106**, 2117–2143 (2018).

14. H. Xu, D. Dai, and Y. Shi, "Silicon integrated nanophotonic devices for on-chip multi-mode interconnects," Appl. Sci. **10**, 6365 (2020).

15. X. Sun, S. Liang, W. Cheng, *et al.*, "Regrowth-free AlGaInAs MQW polarization controller integrated with a sidewall grating DFB laser," Photon. Res. **11**, 622–630 (2023).

16. Z. Wang and D. Dai, "Ultrasmall Si-nanowire-based polarization rotator," J. Opt. Soc. Am. B **25**, 747–753 (2008).

17. H. Fukuda and K. Wada, "Parallel-core-type polarization rotator for silicon wire waveguide platform," Photon. Res. **2**, A14–A18 (2014).

18. H. Wu, Y. Tan, and D. Dai, "Ultra-broadband high-performance polarizing beam splitter on silicon," Opt. Express **25**, 6069–6075 (2017).

19. J. Feng, R. Akimoto, and H. Zeng, "Asymmetric silicon slot-waveguide-assisted polarizing beam splitter," IEEE Photon. Technol. Lett. **28**, 1294–1297 (2016).

20. Y. Zhang, Y. He, J. Wu, *et al.*, "High-extinction-ratio silicon polarization beam splitter with tolerance to waveguide width and coupling length variations," Opt. Express **24**, 6586–6593 (2016).

21. Z. Chen, J. Yang, W.-H. Wong, *et al.*, "Broadband adiabatic polarization rotator-splitter based on a lithium niobate on insulator platform," Photon. Res. **9**, 2319–2324 (2021).

22. J. Wang, B. Niu, Z. Sheng, *et al.*, "Novel ultra-broadband polarization splitter-rotator based on mode-evolution tapers and a mode-sorting asymmetric Y-junction," Opt. Express **22**, 13565–13571 (2014).

23. Y. Xiong, D.-X. Xu, J. H. Schmid, *et al.*, "Fabrication tolerant and broadband polarization splitter and rotator based on a taper-etched directional coupler," Opt. Express **22**, 17458–17465 (2014).

24. Y. Ding, L. Liu, C. Peucheret, *et al.*, "Fabrication tolerant polarization splitter and rotator based on a tapered directional coupler," Opt. Express **20**, 20021–20027 (2012).

25. W. D. Sacher, Y. Huang, L. Ding, *et al.*, "Polarization rotator-splitters and controllers in a Si₃N₄-on-SOI integrated photonics platform," Opt. Express **22**, 11167–11174 (2014).

26. H. Zhou, Y. Zhao, Y. Wei, *et al.*, "All-in-one silicon photonic polarization processor," Nanophotonics **8**, 2257–2267 (2019).

27. Z. Lin, Y. Lin, H. Li, *et al.*, "High-performance polarization management devices based on thin-film lithium niobate," Light Sci. Appl. **11**, 93 (2022).

28. S. An and O.-K. Kwon, "Active control of polarization state of the light in InP waveguide," Opt. Express **27**, 37806–37815 (2019).

29. G. Zhang, J. Y. Haw, H. Cai, *et al.*, "An integrated silicon photonic chip platform for continuous-variable quantum key distribution," Nat. Photonics **13**, 839–842 (2019).

30. J. D. Sarmiento-Merenguel, R. Halir, X. Le Roux, *et al.*, "Demonstration of integrated polarization control with a 40 dB range in extinction ratio," Optica **2**, 1019–1023 (2015).

31. Q. Xu, L. Chen, M. G. Wood, *et al.*, "Electrically tunable optical polarization rotation on a silicon chip using Berry's phase," Nat. Commun. **5**, 5337 (2014).

32. P. Velha, V. Sorianello, M. V. Preite, *et al.*, "Wide-band polarization controller for Si photonic integrated circuits," Opt. Lett. **41**, 5656–5659 (2016).

33. M. Ma, H. Shoman, K. Tang, *et al.*, "Automated control algorithms for silicon photonic polarization receiver," Opt. Express **28**, 1885–1896 (2020).

34. W. Wu, Y. Yu, W. Liu, *et al.*, "Fully integrated CMOS-compatible polarization analyzer," Nanophotonics **8**, 467–474 (2019).

35. Y. Xiong, Y. Wang, R. Zhu, *et al.*, "Twisted black phosphorus-based van der Waals stacks for fiber-integrated polarimeters," Sci. Adv. **8**, eabo0375 (2022).

36. Z. Zhan, M. Cantono, V. Kamalov, *et al.*, "Optical polarization–based seismic and water wave sensing on transoceanic cables," Science **371**, 931–936 (2021).

37. F. Snik, J. Craven-Jones, M. Escuti, *et al.*, "An overview of polarimetric sensing techniques and technology with applications to different research fields," Proc. SPIE **9099**, 90990B (2014).

38. J. Wang, D. Bonneau, M. Villa, *et al.*, "Chip-to-chip quantum photonic interconnect by path-polarization interconversion," Optica **3**, 407–413 (2016).

39. C. Ma, W. D. Sacher, Z. Tang, *et al.*, "Silicon photonic transmitter for polarization- encoded quantum key distribution," Optica **3**, 1274–1278 (2016).

40. J.-W. Kim, S.-H. Park, W.-S. Chu, *et al.*, "Integrated-optic polarization controllers incorporating polymer waveguide birefringence modulators," Opt. Express **20**, 12443–12448 (2012).

41. W. Zhao, R. Liu, Y. Peng, *et al.*, "High-performance silicon polarization switch based on a Mach–Zehnder interferometer integrated with polarization-dependent mode converters," Nanophotonics **11**, 2293–2301 (2022).

42. D. Dai and J. E. Bowers, "Novel concept for ultracompact polarization splitter-rotator based on silicon nanowires," Opt. Express **19**, 10940–10949 (2011).

43. L. Zhang, S. Hong, Y. Wang, *et al.*, "Ultralow-loss silicon photonics beyond the singlemode regime," Laser Photon. Rev. **16**, 2100292 (2022).

44. W. Zhao, Y. Peng, X. Cao, *et al.*, "96-channel on-chip reconfigurable optical add-drop multiplexer for multidimensional multiplexing systems," Nanophotonics **11**, 4299–4313 (2022).

45. D. Dai, C. Li, S. Wang, *et al.*, "10-channel mode (de)multiplexer with dual polarizations," Laser Photon. Rev. **12**, 1700109 (2018).